This article has been accepted for publication in a future issue of this journal, but has not been fully edited. Content may change prior to final publication. Citation information: DOI 10.1109/ACCESS.2020.3028795, IEEE Access

IEEE Access
Multidisciplinary | Rapid Review | Open Access Journal

Date of publication xxxx 00, 0000, date of current version xxxx 00, 0000.

Digital Object Identifier xx.xxxx/ACCESS.yyyy.DOI

A Spatially Adaptive Antenna Array for Mm-Wave Wireless Channel Control with Microfluidics Based Reconfiguration

JONAS MENDOZA[1], MURAT KARABACAK[1,2], HUSEYIN ARSLAN[1,2], (Fellow, IEEE), and GOKHAN MUMCU[1], (Senior Member, IEEE)

[1]Center for Wireless and Microwave Information Systems, University of South Florida, Tampa, FL 33620 USA
[2]School of Engineering and Natural Science, Istanbul Medipol University, 34810 Istanbul, Turkey

Corresponding author: Gokhan Mumcu (e-mail: mumcu@usf.edu).

This work was supported in part by the U.S. National Science Foundation Award #1609581 and in part by the Scientific and Technological Research Council of Turkey (TUBITAK) under Grant 116E078.

ABSTRACT Spatially adaptive antenna array (SAA) is an electronically scanned antenna array with capability of changing its physical location. This new capability allows SAA to control the wireless channel environment to increase link capacity without employing an increased number of antenna elements. Compact and cost-effective implementation of SAA requires a strategically designed RF feed network that can allow the radiating antenna elements to be repositioned while other RF and digital electronics remain stationary. This manuscript introduces a novel RF feed network and demonstrates the first experimental verification of SAA by using microfluidic based reconfiguration. The presented microfluidically reconfigurable SAA (MRSA) exhibits the best possible compact form - a total footprint that is approximately equal to the spatial adaptation range. MRSA operates at 28 GHz with 45 mm (4.2 λ_0) spatial adaptation capability. Evaluating MRSA in communication systems using its measured realized gain patterns show that link level performance of the wireless channel is improved by 24% from 8.5 bps/Hz to 10.5 bps/Hz. Additionally, spectral efficiency is improved by 100% with 5 dB improvement in average signal to interference ratio.

INDEX TERMS Beam steering, channel capacity, diversity methods, microfluidics, millimeter wave communication, phased arrays

I. INTRODUCTION

MM-WAVE communications suffer from high path, propagation and blockage losses. Consequently, mm-Wave wireless networks are planned to be densely deployed [1] while employing high-gain antenna arrays with electronic beam-steering capabilities [2], [3]. Phased antenna arrays (PAAs) are an attractive solution. However, mm-Wave PAAs exhibit high hardware complexity due to dense inter-element spacing, large number of antenna elements, large number of active components, and the need for routing of many RF, bias, and control signals. These challenges motivate novel approaches at hardware integration, packaging, and antenna array architectures. Silicon integrated circuits (ICs) have been demonstrated to support the beam-steering functionalities with high output power and excellent linearity. An example of this can be found in [4] where SiGe technology is employed to realize a 44 GHz transceiver architecture with integrated beam-steering capability for a 4×4 antenna array. Similarly, reference [5] reports a PAA IC for 5G communications based on SiGe BiCMOS technology. Reference [6] addresses the packaging of ICs and antenna arrays by resorting to a hybrid integration approach with multiple printed circuit board (PCB) layers. Other notable techniques being pursued for packaging of PAAs are on-wafer integration [7], heterogeneous integration [8] and additive manufacturing [9], [10]. At the architecture level, subarrays [11]–[13], lens antenna subarrays [14], beam-forming networks [15] and traditional lens antennas [16] are being investigated to reduce the complexity of PAAs.

Different than these approaches, we have recently demonstrated that providing a new spatial adaptation (i.e. changing the physical location) capability for mm-Wave PAAs increases the wireless channel capacity and system signal to interference ratio (SIR) [17]. Fig. 1(a) shows a potential scenario where a spatially adaptive antenna array (SAA) is at the access point of a system. SAA maintains electronic beam-

This article has been accepted for publication in a future issue of this journal, but has not been fully edited. Content may change prior to final publication. Citation information: DOI 10.1109/ACCESS.2020.3028795, IEEE Access

steering capability. Therefore, spatial adaptation adds an additional degree of freedom. By changing its position, SAA at the access point may alter/control the reflections/scattering in the environment to improve channel link capacity and system SIR (i.e. controlling/tailoring of multipath fading [18], [19]). A successful SAA design should consider the following:

- Spatial Adaptation Range: Reference [20] shows that small scale wireless channel changes with antenna location. Changing antenna location by $\lambda_0/2$ (λ_0 denotes free space wavelength) causes received signal to be uncorrelated by 50% with the signal received in previous location – implying a different multipath fading environment. Capability to vary position in many multiples of $\lambda_0/2$ is expected to maximize the possibility of finding a favorable multipath environment for maximizing link capacity and system SIR.
- Physical Size: Array assembly size should be kept close to its spatial adaptation range. A basic approach of connectorization of the antenna elements and utilization of cables for connecting to printed circuit board (PCB) hosting the beam-steering electronics will be bulky, slow and perhaps not suitable in mm-Wave frequencies due to the antenna element spacing.
- Frequency: Since displacements of multiple wavelengths are desired, SAA becomes practical in mm-Wave bands and in applications where multipath fading is still important.
- Speed of Spatial Adaptation: Coherence time defines the time duration where the wireless channel is stable in each antenna location. One of the promising applications of mm-Wave systems is indoor communication [21]. Studies on mm-Wave indoor communication channel characteristics show the coherence time of the channel can be up to 30 ms [22], [23]. Therefore, performing $\lambda_0/2$ motion in less than 30 ms may allow the system to employ better wireless channel conditions.

To satisfy the physical size and speed demands, we propose strategically designed antenna feed networks that allow to move only the antenna metallizations (e.g. patches) while keeping other parts of the array assembly (e.g. active ICs, beamforming ICs, and other frontend/backend electronics) fixed. The earlier work in [17] focused on the wireless system modeling and performance while utilizing simulation-only antenna gain data from a smaller (5 element) SAA that did not satisfy the physical size requirement well. In [17], spatial adaptation range is 4.2 λ_0, but physical assembly length is significantly larger as $9.8\lambda_0$. Actuation of antenna metallizations were planned to be carried out with microfluidics, hence making it a microfluidically reconfigurable SAA (MRSA) motivated by our work that demonstrated highly reconfigurable RF devices [24]–[29]. In addition, the proposed assembly in [17] is not practically implementable for large arrays due to the flexibility of the polymer housing of microfluidic channels, necessitating modifications in assembly and manufacturing. Hence, the main goal of this manuscript

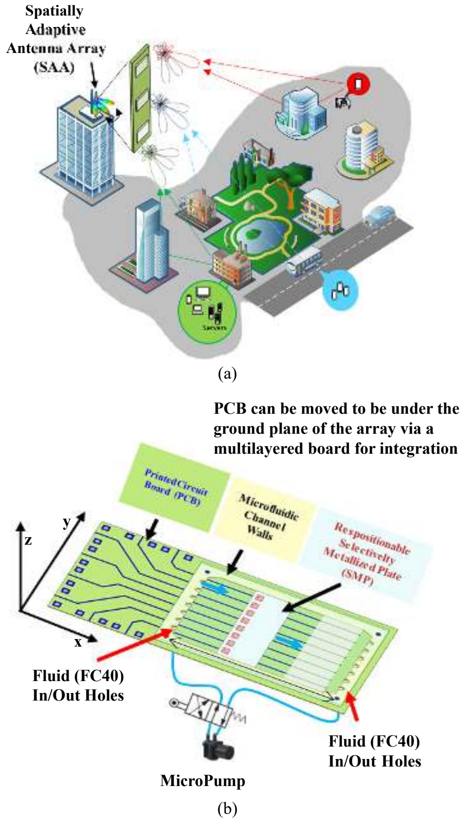

FIGURE 1. Spatially Adaptive antenna Array (SAA) concept: (a) Example application scenario; (b) 3D view of the microfluidically reconfigurable spatially adaptive antenna array (MRSA).

is to design and experimentally characterize a MRSA for the first time by also satisfying the SAA design needs. This is accomplished with following contributions:

- A novel feed network that provides spatial adaptation range of 4.2 λ_0 with minimum physical assembly length of 5.69 λ_0 (Section III). This is enabled by using metallizations on both sides of the selectively metallized plate (SMP) repositioning within the microfluidic channel. As compared to literature [24]–[29], this is the first time SMP is metallized in both sides and for different RF functionality (impedance matching vs. antenna radiation), suggesting new possibilities for future microfluidically reconfigurable RF devices.
- Designing an 8 element MRSA (Section IV) and fabricating (Section V) with a new substrate stack-up (Section II). Hard materials are used due to failure of flexible materials of [17] and reliable actuation with high radiation efficiency (>80%) is accomplished (Section VI).
- Demonstrating improvement in wireless channel link level performance by 24%, system level spectral efficiency by 100%, and average SIR by 5 dB by using measured antenna gain vs. physical location data (Section VII). Since these improvements are achieved without boosting antenna array gain (i.e. 5 dB gain implies 3.2× more antenna elements), SAA offers significant savings in antenna numbers and supporting ICs.

This article has been accepted for publication in a future issue of this journal, but has not been fully edited. Content may change prior to final publication. Citation information: DOI 10.1109/ACCESS.2020.3028795, IEEE Access

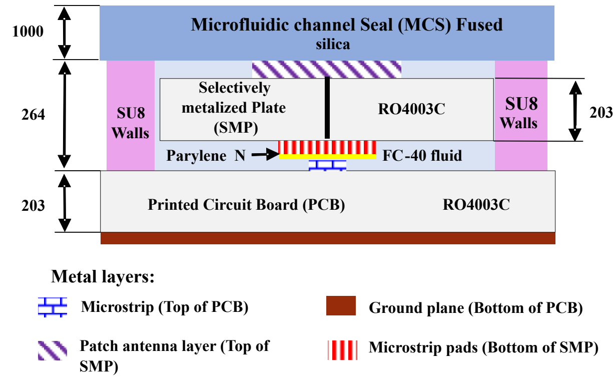

FIGURE 2. Substrate stack-up (all dimensions are in μm).

II. OPERATION PRINCIPLE

Fig. 1(b) depicts the 3D view. Antenna elements are formed over a selectively metallized plate (SMP) that is inside a microfluidic channel. The channel is bonded over a PCB that carries the static section of the RF feed network consisting of 50 Ω microstrip lines. For experimental verification, the lines are extended to mount RF connectors. In a full-scale implementation with beam-steering electronics, more PCB layers can be added under the microfluidic channel to keep the size compact. The patch antennas on the top surface of the SMP are electrically connected to the metallization layer on SMP's bottom surface. The bottom layer transfers RF signals efficiently between the microstrip lines of the PCB and antenna elements while SMP may take any spatial location within the channel. As compared to design of [17], this is a major difference. By realizing a new feed transition on bottom surface of the SMP (but not in the form of a large number of resonators on PCB), the assembly size is significantly reduced. The spatial adaptation of the SMP is achieved by circulating a low-loss dielectric liquid FC40 (ϵ_r = 1.9, tanδ = 0.0005). Although PDMS has been attractive for microfluidically reconfigurable RF devices, high aspect ratio channels needed by the MRSA makes PDMS impossible to use due to flexiblity collapse [30]. The substrate stack-up is therefore formed from hard materials. As shown in Fig. 2, 0.203 mm thick RO4003C laminates (ϵ_r = 3.55 and tanδ = 0.0027) are utilized for realizing both the PCB and SMP. The sidewalls of the channel are implemented from photoresist SU8 (ϵ_r = 3.25 and tanδ = 0.0270). The top wall of the channel is formed with a 1 mm thick fused silica (ϵ_r = 3.81 and tanδ = 0.0002 [31]). The bottom surface of the SMP is coated with a 5 μm thick Parylene-N (ϵ_r = 2.40 and tanδ = 0.0006). This coating enforces a minimum constant gap between the SMP and PCB metallizations and potentially lowers friction. Microfluidic channel walls are 264 μm in total height to accommodate 203 μm thick SMP, 2×17 μm thick SMP metallizations, 5 μm Parylene-Ng, 17 μm thick PCB metallization, and 5 μm FC-40. FC-40 thickness is due to channel height non-uniformity in the fabrication process.

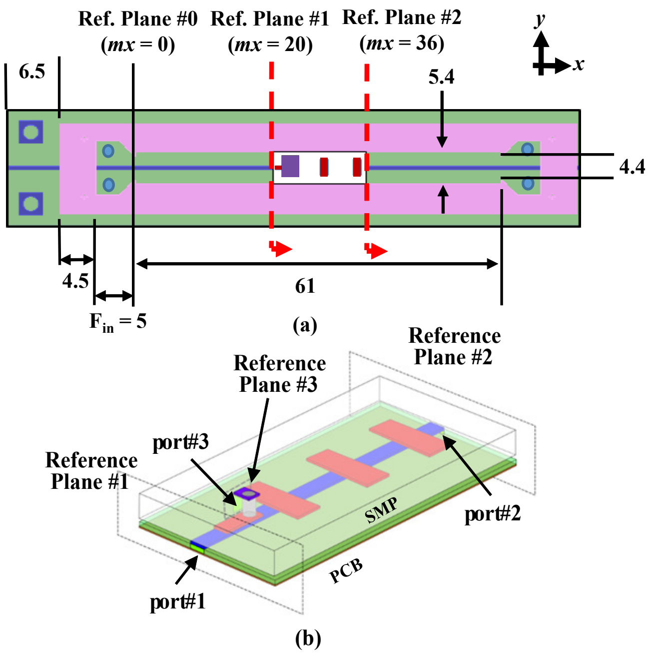

FIGURE 3. (a) Top view of the antenna element; (b) 3D view of the SMP when the patch antenna is replaced with port #3. Dimensions are in mm.

III. DESIGN

Fig. 3(a) shows the top view of the antenna element that is used to form the MRSA. Keysight Advanced Design System (ADS) Momentum suite is employed for the feed network designs. The design is carried out in following steps:

A. STATIC RF FEED NETWORK

The static RF feed network consists of a microstrip line over the PCB. It is partially under the microfluidic channel and sidewalls. The line is designed to exhibit 50 Ω characteristic impedance under each of these substrate stack-ups. Line sections exhibiting different widths are connected to each other as shown in Fig. 4. The line section referred to as TL1 is only over the PCB and exhibits 0.42 mm width. TL2 section lies under the sidewall of the microfluidic channel (SU8 + fused silica). It is in 0.36 mm width and designed using the approach reported in [32]. Its length is 4.5 mm and matches the sidewall width. TL3 section is inside the microfluidic channel filled with FC-40. It is 0.4 mm wide and 61 mm long. TL3 is followed by 4.5 mm long TL2 and 7.44 mm long TL1 sections. The feed network is open-ended. Hence, transition of RF signal from the feed network to the antenna on SMP must prevent signal loss and resonances associated with this type of termination.

B. SMP

SMP has top and bottom surface metallization layers along with a metallized via that electrically connects them to each other. First, the top layer is designed as a patch antenna without the presence of bottom layer (see Fig. 5(a)). The metallized via is replaced with a port referred to as reference plane and port #3. Fig. 3(b) shows for all reference planes

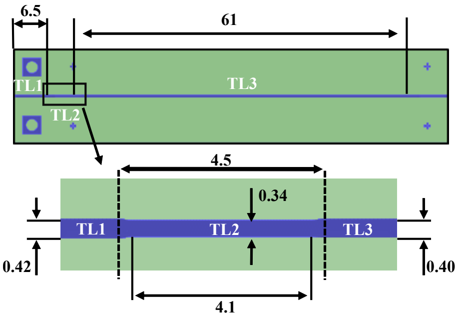

FIGURE 4. Layout of the microstrip feed line. Dimensions are in mm.

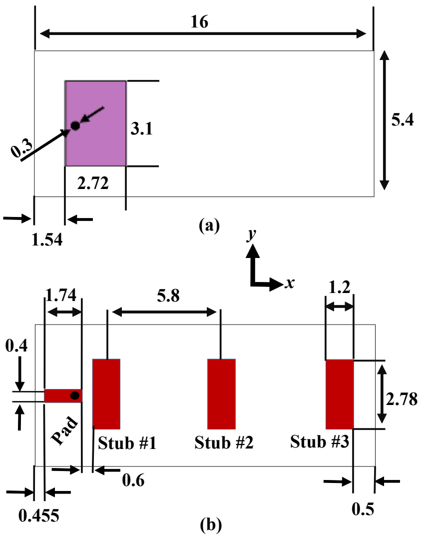

FIGURE 5. SMP layouts: (a) Top; (b) Bottom. Dimensions are in mm.

and ports. Dimensions are tuned to achieve a resistive input impedance of 30 Ω. Replacing the port with 0.3 mm diameter metallized via and capacitive coupling between the SMP bottom metallization layer and PCB microstrip line transforms this impedance to 50 Ω at the reference plane #1. Fig. 5(b) depicts the bottom layer. A pad overlaps with the 0.4 mm wide microstrip line on the PCB to pick up the RF signal through capacitive coupling. There are stubs that periodically load the microstrip line on the PCB. These stubs act as an RF block mechanism to prevent resonances of the open-ended microstrip line on the PCB. The design is carried out based on S-parameter analysis of a three-port network where the patch antenna is represented with 30 Ω port #3. The design goal is to maximize $|S_{31}|$ while minimizing $|S_{11}|$ and $|S_{21}|$. The length of the pad is designed when no stubs are present. Fig. 6(a) presents $|S_{31}|$, $|S_{21}|$ and $|S_{11}|$ at 28 GHz for various pad lengths. Reflected power is minimized for 1.74 mm pad length. However, $|S_{31}|$ is only -3.6 dB, implying a large amount of RF signal leakage from reference plane #1 to #2. $|S_{21}|$ of the network confirms this by being -3.8 dB. To minimize the leakage, stub #1 is included. It is 1.39 mm in length, which represents a 0.25 λ_g guided wavelength at 28 GHz. The stub approximates a short circuit condition on the microstrip line of the PCB. Initial stub width is 0.36 mm

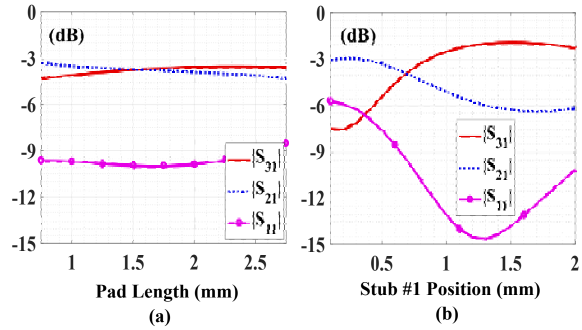

FIGURE 6. S-parameters at 28 GHz as a function of (a) pad length and (b) stub #1 position relative to the pad.

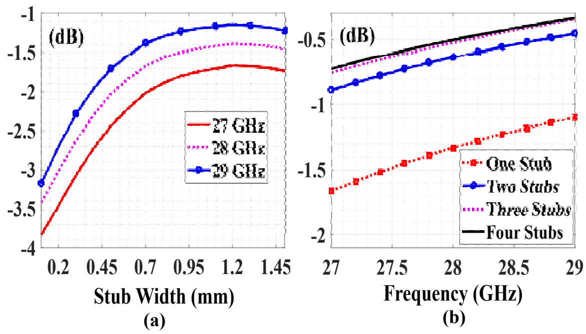

FIGURE 7. $|S_{31}|$ as a function of (a) stub #1 width; (b) frequency.

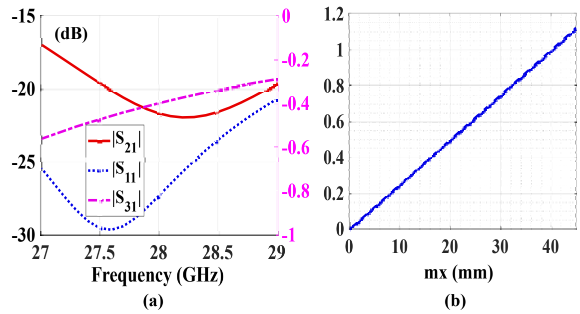

FIGURE 8. (a) S-parameters with finalized SMP layouts; (b) Feed network insertion loss vs *mx* at 28 GHz.

corresponding to a 50 Ω impedance. A parametric study on stub #1 position as depicted in Fig. 6(b) shows that reflected power is minimized when stub #1 is 1.25 mm separated from the pad. As expected, this is close to a quarter-wavelength and transforms the short-circuit condition realized by the stub #1 to an open-circuit condition at the pad location. Fig. 7 (a) presents $|S_{31}|$ performance for varying stub widths. 1.2 mm wide stub maximizes the $|S_{31}|$. Stub #1 improves $|S_{31}|$ from -3.6 dB to -1.38 dB at 28 GHz. Inclusion of other stubs that are separated from each other by 5.8 mm (i.e. λ_g) further improves $|S_{31}|$. Fig. 7(b) depicts the $|S_{31}|$ when the number of stubs is varied from one to four. Addition of the fourth stub affects the $|S_{31}|$ minimally. Consequently, the layout of the SMP is finalized with three stubs. Fig. 8 (a) presents the $|S_{21}|$, $|S_{11}|$, and $|S_{31}|$ for the finalized SMP layouts. The insertion loss between reference planes #1 and #3 is less than 0.4

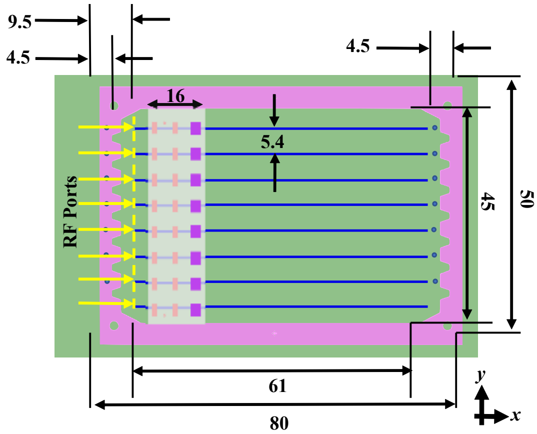

FIGURE 9. Eight Element MRSA layout.

dB at 28 GHz with return losses exceeding 20 dB. Fig. 8 (b) depicts the insertion loss of the feed network at 28 GHz as a function of mx between reference plane #0 and #1. Loss linearly increases with mx as would be expected from a well-matched transmission line. Insertion loss remains below 1.1 dB and SMP can take any position.

IV. MRSA

MRSA design is shown in Fig. 9. PCB and SMP widths are enlarged to accommodate replicas of the microstrip feed lines and SMP metallizations to include 8 antenna elements. Antenna elements are evenly spaced with 5.4 mm ($\lambda_0/2$). Microfluidic channel is enlarged to host the 16 $\times$ 45 mm^2 SMP. The overall size is 80 $\times$ 50 mm^2, excluding the extension lines that are connectorized for experimental purpose. The radiation performance of the MRSA is simulated using Ansys HFSS. Each microstrip feed line is excited by a 50 Ω lumped port. Fig. 10 demonstrates $|S_{11}|$ of an antenna element as the array is repositioned across the microfluidic channel from mx = 0 mm to mx = 45 mm. $|S_{11}|$ is < -12 dB within the 27 GHz – 29 GHz frequency band. Simulated radiation efficiency is 84% at 28 GHz when the SMP is located at its closest position to the feed ports, i.e., mx = 0 mm. The radiation efficiency is due to the dielectric loss of the materials (3.6%), conductor losses (3.6%) and the 0.4 dB insertion loss of the feed network to antenna transition (8.8%). Uniformly excited MRSA exhibits 14.86 dBi realized gain at 28 GHz with 12° half power beam width (HPBW) in the H-plane and less than -5 dBi back radiation gain. The E-plane HPBW is 48°.

Fig. 11(a) depicts the beam-steering in 12° increments in H-plane when mx = 0 mm. H-plane realized gain pattern can be scanned from -48° to 48° with a gain loss below 2.35 dB. Side lobe level is less than -12 dB. Fig. 11(b) depicts the broadside gain of the MRSA for 0°, 24°, and 48° scan directions at 28 GHz as the SMP is repositioned within the microfluidic channel. The simulated realized broadside gain is worst for the 48° direction and remains > 9 dBi for all scan directions including the ones not shown. The realized

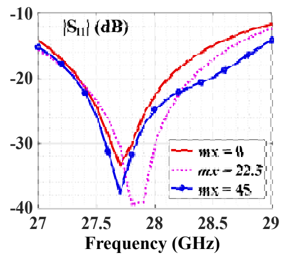

FIGURE 10. $|S_{11}|$ of a single element of the array for different *mx*.

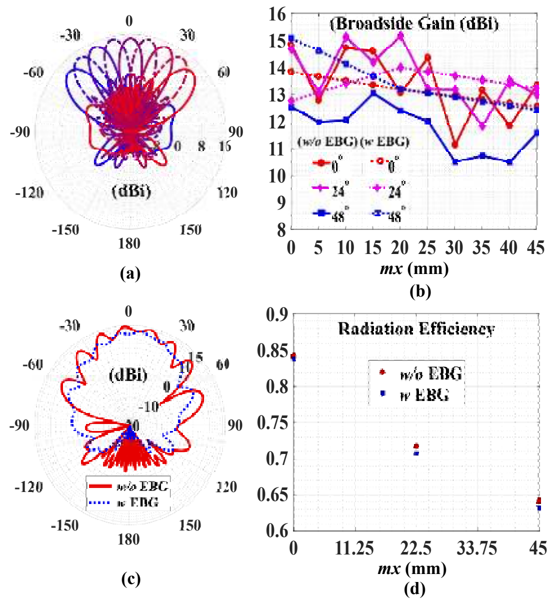

FIGURE 11. (a) Realized gain pattern at 28 GHz for eight different steering angles in the H-plane (y-z) plane for *mx* = 0 mm; (b) Broadside realized gain vs SMP displacement for 0°, 24°, and 48° beam steering at 28 GHz with and without EBG; (c) Realized gain pattern in the E-plane at *mx* = 0mm; (d) Radiation efficiency for different *mx* positions.

gain of the 48° scan is primarily associated with the expected scan loss. The broadside gain varies by ± 1 dB of an average level. This is associated with the electrically large ground plane size of the array. As shown in Fig. 11(c), E-plane radiation pattern of the antenna exhibits ripples similar to the cases reported in previous literature [33], [34], implying contributions of scattered fields. As the array is repositioned, these contributions vary.

Electromagnetic band gap structures (EBG) can improve the E-plane radiation pattern affected by surface wave refraction [35]–[37]. As shown in Fig. 12(a), EBG can be placed within the side walls of the microfluidic channel. EBG unit cell is modeled in Ansys HFSS with the eigenmode solver. It is 2×2 mm^2 and consists of a 0.3 mm diameter metallized via. The unit cell height is 1.467 mm and covers the entirety of the substrate stack-up. The dispersion diagram in Fig. 12(b) shows that the design exhibits a band gap between 25 GHz and 40 GHz. With EBGs, the gain ripples can be eliminated as seen in Fig. 11(c). Broadside gain also gets stabilized with respect to mx as shown in Fig. 11(b). Fig. 11(d) presents the simulated radiation efficiencies for

This article has been accepted for publication in a future issue of this journal, but has not been fully edited. Content may change prior to final publication. Citation information: DOI 10.1109/ACCESS.2020.3028795, IEEE Access

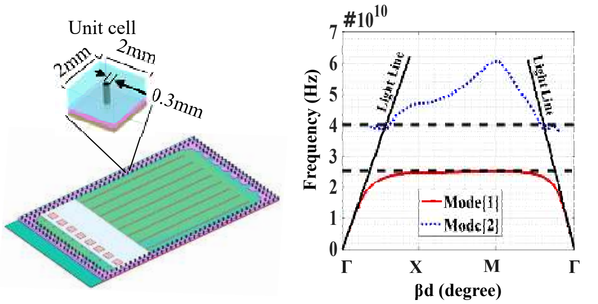

(a) (b)

FIGURE 12. (a) MRSA with EBGs in microfluidic channel walls; (b) Dispersion diagram for the EBG.

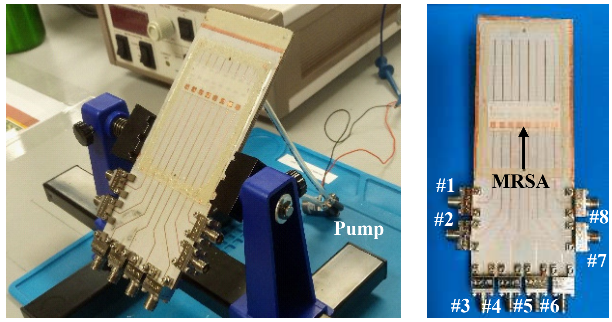

Isometric View Top View

FIGURE 13. Experiment setup for the MRSA.

both approaches. Inclusion of EBGs cause only 1% reduction in radiation efficiency. Drop in radiation efficiency with mx is associated with increasing feed network loss.

Fabrication of metallized vias through fused silica substrate is out of the current capabilities of our laboratory. Hence, the experimental characterization is carried out without the EBGs. Nevertheless, the wireless communication system evaluation in Section VII based on measured antenna performance still shows significant benefits arising due to the proposed spatial adaptation capability. This improvement is expected since the wireless channel gain observed in different mx positions exhibit statistically distributed fading (i.e. channel gain fluctuations). Hence, multiplication of antenna gain and wireless channel gain that governs the overall system performance always exhibits statistically distributed ripples even if the MRSA gain is smoothed out with inclusion of EBGs. Therefore, at the system level, small ± 1 dB gain ripples related to the surface wave scattering are not critical for the overall performance.

V. FABRICATION

Microfluidically reconfigurable RF devices with hard channel walls are not commonly pursued as compared to flexible material based approaches such as PDMS [38]. Among the limited work, reference [39] uses laser machined Poly Methyl Methacrylate (PMMA) and bonds it with a inkjet-printed photo-paper substrate. The bonding is performed by using inkjet printed SU8 as a glue agent. Similarly, [40] uses a silica-based superhydrophobic coated PMMA as microfluidic channel material on a liquid metal based reconfigurable antenna. The bonding is performed by using a Norland Optical Adhesive-63 glue. Likewise, [41] proposes a frequency reconfigurable slot antenna enabled by liquid metal actuation inside a S-glass microfluidic channel. These are different from the substrate stack-up utilized in this work. Most recently, in [29], we used a substrate stack-up that is similar to the one in this paper. Due to the brevity of [29], fabrication details were not given. In addition, the size and aspect ratios of the channels for MRSA is very large, hence, making its manufacturing details critical for repeatability.

The PCB and SMP are patterned using standard photolithography, hence, these details are omitted for brevity. The microfluidic channel sidewalls are constructed with photoresist SU8-2075. The 0.203 mm thick PCB is first bonded with a 1.5 mm thick RO4003C substrate to reduce its flexibility. Subsequently, it is spin-coated with a 254 µm thick layer of SU8 in two spin-coating steps. First SU8 layer is spin coated at 1500 rpm for 45 s and soft baked for 25 min at 95 °C. The second SU8 layer is spin coated at 2200 rpm for 45 s and then soft baked for 45 min at 95 °C. The spin coating process is followed by a 400 mJ/cm^2 UV exposure and a three steps of post-exposure baking profile. The first section of the baking profile keeps the PCB at 60 °C for 7 min. The second step ramps the temperature up to 90 °C in 20 min. The final step cools down the PCB to room temperature. The application of multiple SU8 coatings and the utilized temperature profile reduces deformation and planarizes the SU8 walls. Profilometer characterizations demonstrate a ±10 µm height variation across the SU8 layer. The final step in preparation of microfluidic channel walls is the development of the SU8 layer and rinsing of the PCB substrate.

The channel sidewalls are bonded with the fused silica using the adhesive bonding technique described in [42]. First, a 20 µm thick SU8 layer is spin coated on top of a polymide surface. Subsequently, spin coated polyimide surface is brought in contact with the sidewalls of the microfluidic channel to transfer uncured SU8 from polymide surface to the top surface of the sidewalls (i.e. contact imprinting). Next, the PCB with the thin SU8 bonding layer is kept at 60 °C for 10 min to minimize the SU8 viscosity and leaking into the channel during contact bonding with the fused silica. The fused silica substrate is then pressed against the microfluidic channel and kept at 90 °C for 2 min. Fig. 13(b) show the MRSA prototype. The liquid FC40 is actuated by a TCS M100 pump through the fluid in/out holes at the back of the PCB structure. 3 mm internal diameter Teflon pipes and valves connect the pump to the microfluidic channel. The entry points to the microfluidic channel are fitted with PDMS based adapters as used in our previous work [43].

VI. EXPERIMENTAL VERIFICATION

Reconfiguration speed of the prototype is characterized as 14.3 λ_0/s (154 mm/s) which implies 35 ms per $\lambda_0/2$ displacement. The speed is achieved with 2 V DC voltage. It is possible to attain $\lambda_0/2$ displacement in 15 ms with the

This article has been accepted for publication in a future issue of this journal, but has not been fully edited. Content may change prior to final publication. Citation information: DOI 10.1109/ACCESS.2020.3028795, IEEE Access

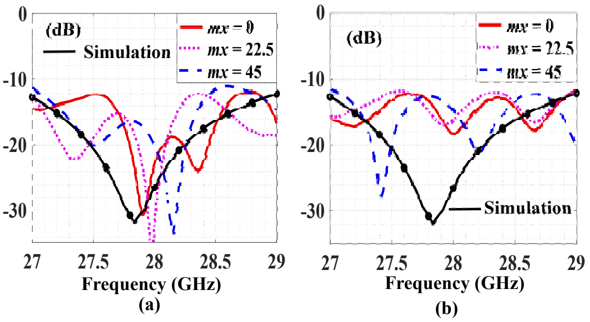

FIGURE 14. Measured $|S_{11}|$: (a) Element #3; (b) Element #1.

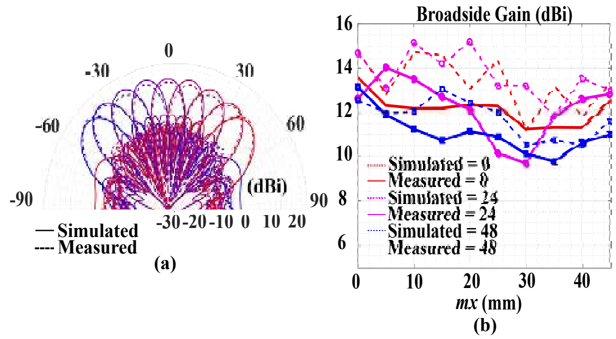

FIGURE 15. (a) Realized gain pattern for *mx* = 0mm; (b) Broadside realized gain vs *mx* for multiple beam steering directions.

maximum pump capacity achieved at 3 V DC voltage. However, for our set-up, increased speed has caused unreliability in PDMS/tube adapters. Future prototypes can utilize larger peripheral pipes and liquid in/out ports to improve reliability at the PDMS/tube adapters. These actuation times are suitable for indoor communications as explained in introduction.

Fig. 14(a) and (b) present $|S_{11}|$ of elements #3 and #1 since they are connected to their own RF edge connectors with the shortest and longest transmission lines, respectively. The difference between the simulated and measured $|S_{11}|$ is primarily due to the TL1, TL2 and RF edge connectors that were not included in the simulations. In addition, fabrication tolerances/errors may contribute to the differences. Nevertheless, all antenna elements in the MRSA prototype (including the elements whose $|S_{11}|$ are not shown for brevity) are well-matched with $|S_{11}|$ below -10 dB.

Fig. 15(a) depicts the measured realized gain of the MRSA at 28 GHz for different beam-steering angles in the mx = 0 position. The radiation pattern of each antenna element is measured while other elements are terminated with 50 Ω loads. The measured radiated fields of the antenna elements are summed in software with phase shifts to generate beam-steering in H-plane with 12° increments. The phase delay and insertion loss of the microstrip extension lines used to make connection with the edge connectors are calculated with Keysight ADS and compensated for in the radiated field summation. Edge connectors exhibit 0.5 dB insertion loss in this frequency range and this is accounted for in the radiation pattern summation as well. As shown in Fig. 15(a), simulated and measured realized gain values are in good agreement. MSRA exhibits 14 dBi measured realized broadside gain at 28 GHz for mx = 0 and 12° HPBW in the H-plane. Fig. 15(b) compares simulated and measured 28 GHz broadside realized gains of the MSRA for 0°, 24°, and 48° beam-steering angles at different mx. The array shows a realized gain higher than 9 dBi for all the beam-steering angles including the ones not shown here. The average variation between the measured and simulated realized gain is 1.08 dBi. This difference can be related to slight misalignments in fabrication and anechoic chamber measurements. In addition, the ground plane size for the prototype is larger than the simulated model (see Fig. 1(b) vs. Fig. 12) due to the inclusion of connectors.

VII. SYSTEM EVALUATION

To demonstrate the advantages of MRSA, wireless system and link level performance simulations are carried out based on the measured H-plane gain patterns obtained from the MRSA prototype at varying mx positions. Measured H-plane gain patterns include all the nonidealities stemming from the feed network losses and realized gain variations as a function of mx. Hence, presented system evaluation provides insight for performance under realistic/practical situations. Simulations follow a similar approach to [17]. Path loss model is assumed as PL(dB) = 72 + 29.2log10(d) based on [44], where d is the distance between transmitter and transmitter. First, link level simulations are performed in a scattering environment. Up to 4 scatterers are randomly placed with Poisson distribution to generate a multipath channel in 800 $\lambda_0 \times$ 800 λ_0 area between the transmitter and receiver. Only the transmitter is assumed to be equipped with the MRSA whereas the receiver antenna is omnidirectional. The transmitter beam and location is selected to maximize the received signal strength. Assuming a noise floor of -174 dBm, spectral efficiency of the wireless channel link is calculated. Fig. 16(a) presents the link level spectral efficiency when the transmitter is equipped with omni directional antenna, traditional 8 element beam-steering array (i.e. MRSA prototype in its best position closest to the feed points) and the 8 element MRSA prototype with spatial adaptation capability. MRSA increases the spectral efficiency with its spatial adaptation range. For 4.2 λ_0 spatial adaption range, MRSA achieves 24% more spectral efficiency. In the wireless system simulation, 50 base stations with their attached users are spread in 200 $\times$ 200 m^2 area. The channel and path loss is generated based on models given in [44] while the transmit power of the base stations are considered as 30 dBm. Each base station is assumed to be selfish and maximizes the spectral efficiency of its own users. The maximization algorithm simply calculates the spectral efficiency based on signal to interference rates (SIR) of available beam and spatial displacement options and selects the maximum. Thus, the algorithm does not only aim to increase receive power but also minimize interference. Fig. 16(b) shows cumulative distribution of spectral efficiency for the users in the system. Equipping the base stations with the MRSAs provide 100%

This article has been accepted for publication in a future issue of this journal, but has not been fully edited. Content may change prior to final publication. Citation information: DOI 10.1109/ACCESS.2020.3028795, IEEE Access

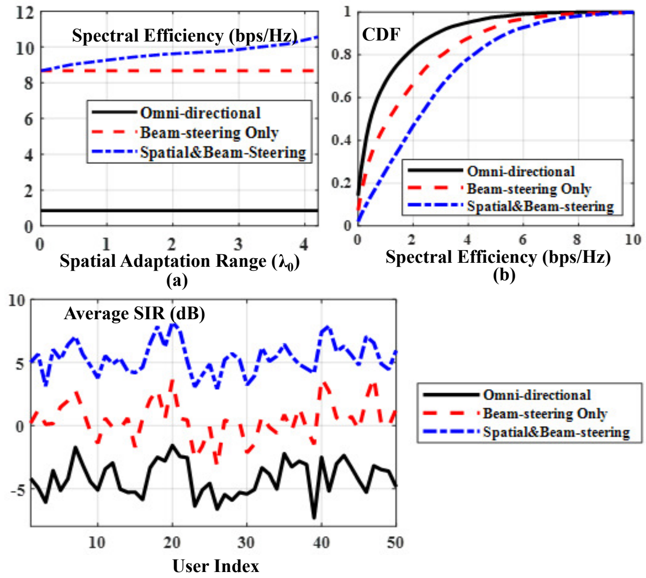

(c)

FIGURE 16. (a) Link level spectral efficiency vs. spatial adaptation range; (b) Cumulative distribution of spectral efficiency in wireless network for users; (c) Instantaneous SIR values of the user in the network while MRSA ('Spatial and Beam-Steering' arrays) exhibit maximum 4.2 λ_0 spatial adaptation.

gain in average spectral efficiency. The gain in system level simulation is significantly higher than the link level gain since MRSA provides an additional diversity for interference management, while link level evaluation assumes no interference in the environment. Fig. 16(c) gives instantaneous SIR values of the users and it is clearly seen that the proposed approach provides an average 5 dB SIR gain in the system.

A conventional approach to increase signal level by 5 dB would be to increase the gain of the antenna array by 5 dB. From effective aperture area consideration, this would require employing 3.2× area and antenna elements. Therefore, in a full-scale implementation that will include beam-steering electronics, 3.2× antenna elements will need to be supported by corresponding electronics such as beamforming integrated circuits, RF feed networks and bias/control lines – significantly increasing the implementation complexity. On the other hand, we show that spatial adaptation provides this improvement without increase in antenna numbers and corresponding electronics. Table 1 presents a comparison between the presented MRSA and the simulation only one reported in earlier work [17]. In addition, the table includes performance comparison with several conventional PAAs reported in literature [17], [45]–[51]. It is observed that presented MRSA is significantly improved in assembly size and experimentally verified as compared to [17]. It is also seen that the radiation efficiency and realized gain of the MRSA is comparable to other antenna arrays. This verifies that spatial adaptation can be used as an additional degree of freedom in wireless systems.

TABLE 1. Performance comparison

Ref.	Effic. %	Max. Realized. Gain $[dBi]$	Spatial Adapt. Range	Assembly Length	Element Count	Avg. SIR gain
This work	84	14 Measured	4.2 λ_0	61 mm	1×8	5dB
[17]	80	11.1 Simulated	4.2 λ_0	105 mm	1×5	3dB
[45]	83	14.0	–	–	1×8	–
[46]	72	14.5	–	–	1×8	–
[47]	76.8	14.96	–	–	1×8	–
[48]	65	21	–	–	4×8	–
[49]	50	28.4	–	–	[4×6]×8	–
[50]	72	12.2	–	–	1×4	–
[51]	80	12.5	–	–	1×8	–

VIII. CONCLUDING REMARKS

This paper demonstrated a compact microfluidically reconfigurable spatially adaptive planar antenna array (MRSA) operating at 28 GHz. Array exhibits 45 mm (4.2 λ_0) spatial adaptation capability with a 61 mm long microfluidic channel. MRSA is well-matched for all possible spatial positions due to its feed network design. It exhibits 14 dBi peak realized broadside gain and 12° H-plane HPBW. It was shown that MRSA provides spatial diversity to improve received power while also giving opportunity to reduce interference. Specifically, link level performance of a wireless channel can be improved by 24% from 8.5 bps/Hz to 10.5 bps/Hz. System level average spectral efficiency was improved by 100%. In addition, 5 dB improvement in average signal to interference ratio was achieved. Future work will consider extending the presented approach into 2D antenna arrays by resorting to meandered and miniaturized feed network architectures in multilayered substrate stack-ups.

REFERENCES

[1] S. A. Busari, S. Mumtaz, K. M. S. Huq, J. Rodriguez, and H. Gacanin, "System-level performance evaluation for 5g mmwave cellular network," in *GLOBECOM 2017 - 2017 IEEE Global Communications Conference*, 2017, pp. 1–7.

[2] G. E. Bottomley, *Channel Equalization for Wireless Communications: From Concepts to Detailed Mathematics*, 2011, pp. i–xxvii.

[3] Q. Xue, P. Zhou, X. Fang, and M. Xiao, "Performance analysis of interference and eavesdropping immunity in narrow beam mmwave networks," *IEEE Access*, vol. 6, pp. 67 611–67 624, 2018.

[4] J. Hacker, C. Hillman, A. Papavasiliou, Chong Gon Kim, A. Abbaspour-Tamijani, C. Y. Kim, D. W. Kang, and G. Rebeiz, "A 16-element transmit/receive q-band electronically steerable subarray tile," in *2012 IEEE/MTT-S International Microwave Symposium Digest*, 2012, pp. 1–3.

[5] B. Sadhu, Y. Tousi, J. Hallin, S. Sahl, S. K. Reynolds, . Renström, K. Sjögren, O. Haapalahti, N. Mazor, B. Bokinge, G. Weibull, H. Bengtsson, A. Carlinger, E. Westesson, J. Thillberg, L. Rexberg, M. Yeck, X. Gu, M. Ferriss, D. Liu, D. Friedman, and A. Valdes-Garcia, "A 28-ghz 32-element trx phased-array ic with concurrent dual-polarized operation and orthogonal phase and gain control for 5g communications," *IEEE Journal of Solid-State Circuits*, vol. 52, no. 12, pp. 3373–3391, 2017.

[6] J. Wu, Y. J. Cheng, and Y. Fan, "A wideband high-gain high-efficiency hybrid integrated plate array antenna for v-band inter-satellite links," *IEEE Transactions on Antennas and Propagation*, vol. 63, no. 4, pp. 1225–1233, 2015.

[7] O. Bayraktar, O. A. Civi, and T. Akin, "Beam switching reflectarray monolithically integrated with rf mems switches," *IEEE Transactions on Antennas and Propagation*, vol. 60, no. 2, pp. 854–862, 2012.

[8] C. Li, T. Chao, C. Lai, W. Chen, C. Ko, C. Kuo, Y. T. Cheng, M. Kuo, and D. Chang, "A 37.5-mw 8-dbm-eirp 15.5°-hpbw 338-ghz terahertz trans-

mitter using sop heterogeneous system integration," *IEEE Transactions on Microwave Theory and Techniques*, vol. 63, no. 2, pp. 470–480, 2015.

[9] E. A. Rojas-Nastrucci, R. Ramirez, D. Hawatmeh, D. Lan, J. Wang, and T. Weller, "Laser enhanced direct print additive manufacturing for mm-wave components and packaging," in *2017 International Conference on Electromagnetics in Advanced Applications (ICEAA)*, 2017, pp. 1531–1534.

[10] M. Kacar, J. Wang, G. Mumcu, C. Perkowski, K. Church, B. Wu, and T. Weller, "Phased array antenna element with embedded cavity and mmic using direct digital manufacturing," in *2019 IEEE International Symposium on Antennas and Propagation and USNC-URSI Radio Science Meeting*, 2019, pp. 81–82.

[11] Y. Tsai, Y. Chen, and R. Hwang, "Combining the switched-beam and beam-steering capabilities in a 2-d phased array antenna system," *Radio Science*, vol. 51, no. 1, pp. 47–58, 2016.

[12] A. Abbaspour-Tamijani and K. Sarabandi, "An affordable millimeter-wave beam-steerable antenna using interleaved planar subarrays," *IEEE Transactions on Antennas and Propagation*, vol. 51, no. 9, pp. 2193–2202, 2003.

[13] F. Akbar and A. Mortazawi, "Scalable phased array architectures with a reduced number of tunable phase shifters," *IEEE Transactions on Microwave Theory and Techniques*, vol. 65, no. 9, pp. 3428–3434, 2017.

[14] G. Mumcu, M. Kacar, and J. Mendoza, "Mm-wave beam steering antenna with reduced hardware complexity using lens antenna subarrays," *IEEE Antennas and Wireless Propagation Letters*, vol. 17, no. 9, pp. 1603–1607, 2018.

[15] C. Chang, R. Lee, and T. Shih, "Design of a beam switching/steering butler matrix for phased array system," *IEEE Transactions on Antennas and Propagation*, vol. 58, no. 2, pp. 367–374, 2010.

[16] D. F. Filipovic, S. S. Gearhart, and G. M. Rebeiz, "Double-slot antennas on extended hemispherical and elliptical silicon dielectric lenses," *IEEE Transactions on Microwave Theory and Techniques*, vol. 41, no. 10, pp. 1738–1749, 1993.

[17] M. H. Yılmaz, E. Güvenkaya, G. Mumcu, and H. Arslan, "Millimeter-wave wireless channel control using spatially adaptive antenna arrays," *IEEE Communications Letters*, vol. 21, no. 3, pp. 680–683, 2017.

[18] D. Abu-Al-Nadi, T. Ismail, and M. Mismar, "Interference suppression by element position control of phased arrays using lm algorithm," *AEU - International Journal of Electronics and Communications*, vol. 60, no. 2, pp. 151 – 158, 2006.

[19] F. Tokan and F. Güneş, "Interference suppression by optimising the positions of selected elements using generalised pattern search algorithm," *IET Microwaves, Antennas Propagation*, vol. 5, no. 2, pp. 127–135, 2011.

[20] M. K. Samimi, S. Sun, and T. S. Rappaport, "Mimo channel modeling and capacity analysis for 5g millimeter-wave wireless systems," in *2016 10th European Conference on Antennas and Propagation (EuCAP)*, 2016, pp. 1–5.

[21] B. Ai, K. Guan, R. He, J. Li, G. Li, D. He, Z. Zhong, and K. M. S. Huq, "On indoor millimeter wave massive mimo channels: Measurement and simulation," *IEEE Journal on Selected Areas in Communications*, vol. 35, no. 7, pp. 1678–1690, 2017.

[22] S. Guillouard, G. El Zein, and J. Citerne, "Wideband propagation measurements and doppler analysis for the 60 ghz indoor channel," in *1999 IEEE MTT-S International Microwave Symposium Digest (Cat. No.99CH36282)*, vol. 4, 1999, pp. 1751–1754 vol.4.

[23] N. Moraitis and P. Constantinou, "Indoor channel measurements and characterization at 60 ghz for wireless local area network applications," *IEEE Transactions on Antennas and Propagation*, vol. 52, no. 12, pp. 3180–3189, 2004.

[24] E. González and G. Mumcu, "Millimeter-wave beam-steering focal plane arrays with microfluidically switched feed networks," *IEEE Transactions on Antennas and Propagation*, vol. 66, no. 12, pp. 7424–7429, 2018.

[25] A. A. Gheethan, M. C. Jo, R. Guldiken, and G. Mumcu, "Microfluidic based ka-band beam-scanning focal plane array," *IEEE Antennas and Wireless Propagation Letters*, vol. 12, pp. 1638–1641, 2013.

[26] A. Dey, R. Guldiken, and G. Mumcu, "Microfluidically reconfigured wideband frequency-tunable liquid-metal monopole antenna," *IEEE Transactions on Antennas and Propagation*, vol. 64, no. 6, pp. 2572–2576, 2016.

[27] T. Palomo and G. Mumcu, "Frequency-agile rf filters using microfluidically reconfigurable selectively metallized plates," in *2017 IEEE Radio and Wireless Symposium (RWS)*, 2017, pp. 1–4.

[28] A. Qaroot and G. Mumcu, "Microfluidically reconfigurable reflection phase shifter," *IEEE Microwave and Wireless Components Letters*, vol. 28, no. 8, pp. 684–686, 2018.

[29] E. González and G. Mumcu, "Integrated actuation of microfluidically reconfigurable mm-wave spst switches," *IEEE Microwave and Wireless Components Letters*, vol. 29, no. 8, pp. 541–544, 2019.

[30] C. Kim, H. Chun, J. Chung, K. Song, and S. Lee, "Non-collapsible pdms nanochannel fabrication with tunable width and height using single master mold," in *2011 11th IEEE International Conference on Nanotechnology*, 2011, pp. 1723–1727.

[31] H. E. Bussey, J. E. Gray, E. C. Bamberger, E. Rushton, G. Russell, B. W. Petley, and D. Morris, "International comparison of dielectric measurements," *IEEE Transactions on Instrumentation and Measurement*, vol. IM-13, no. 4, pp. 305–311, 1964.

[32] A. A. Gheethan, A. Dey, and G. Mumcu, "Passive feed network designs for microfluidic beam-scanning focal plane arrays and their performance evaluation," *IEEE Transactions on Antennas and Propagation*, vol. 63, no. 8, pp. 3452–3464, 2015.

[33] T. Namiki, Y. Murayama, and K. Ito, "Improving radiation-pattern distortion of a patch antenna having a finite ground plane," *IEEE Transactions on Antennas and Propagation*, vol. 51, no. 3, pp. 478–482, 2003.

[34] J. Huang, "The finite ground plane effect on the microstrip antenna radiation patterns," *IEEE Transactions on Antennas and Propagation*, vol. 31, no. 4, pp. 649–653, 1983.

[35] A. Kumar, J. Mohan, and H. Gupta, "Surface wave suppression of microstrip antenna using different ebg designs," in *2015 International Conference on Signal Processing and Communication (ICSC)*, 2015, pp. 355–359.

[36] N. Llombart, A. Neto, G. Gerini, and P. de Maagt, "Planar circularly symmetric ebg structures for reducing surface waves in printed antennas," *IEEE Transactions on Antennas and Propagation*, vol. 53, no. 10, pp. 3210–3218, 2005.

[37] R. Gonzalo, P. De Maagt, and M. Sorolla, "Enhanced patch-antenna performance by suppressing surface waves using photonic-bandgap substrates," *IEEE Transactions on Microwave Theory and Techniques*, vol. 47, no. 11, pp. 2131–2138, 1999.

[38] T. Palomo and G. Mumcu, "Microfluidically reconfigurable microstrip line combline filters with wide frequency tuning capabilities," *IEEE Transactions on Microwave Theory and Techniques*, vol. 65, no. 10, pp. 3561–3568, 2017.

[39] S. Choi, W. Su, M. M. Tentzeris, and S. Lim, "A novel fluid-reconfigurable advanced and delayed phase line using inkjet-printed microfluidic composite right/left-handed transmission line," *IEEE Microwave and Wireless Components Letters*, vol. 25, no. 2, pp. 142–144, 2015.

[40] V. Bharambe, J. J. Adams, I. D. Joshipura, H. R. Ayers, and M. D. Dickey, "Reversibly reconfigurable liquid metal patch antenna using a superhydrophobic spray-coating," in *2018 IEEE International Symposium on Antennas and Propagation USNC/URSI National Radio Science Meeting*, 2018, pp. 287–288.

[41] A. J. King, J. F. Patrick, N. R. Sottos, S. R. White, G. H. Huff, and J. T. Bernhard, "Microfluidically switched frequency-reconfigurable slot antennas," *IEEE Antennas and Wireless Propagation Letters*, vol. 12, pp. 828–831, 2013.

[42] L. Yu, C. Iliescu, F. e. h. Tay, and B. Chen, "Su8 adhesive bonding using contact imprinting," in *2006 International Semiconductor Conference*, vol. 1, 2006, pp. 189–192.

[43] A. Dey and G. Mumcu, "Microfluidically controlled metalized plate based frequency reconfigurable monopole for high power rf applications," in *2015 IEEE International Symposium on Antennas and Propagation USNC/URSI National Radio Science Meeting*, July 2015, pp. 2299–2300.

[44] S. Rangan, T. S. Rappaport, and E. Erkip, "Millimeter-wave cellular wireless networks: Potentials and challenges," *Proceedings of the IEEE*, vol. 102, no. 3, pp. 366–385, March 2014.

[45] N. Ojaroudiparchin, M. Shen, and G. F. Pedersen, "Low-cost planar mm-wave phased array antenna for use in mobile satellite (msat) platforms," in *2015 23rd Telecommunications Forum Telfor (TELFOR)*, Nov 2015, pp. 528–531.

[46] M. Islam, M. Ibrahimy, S. Motakabber, A. K. M. Z. Hossain, and S. M. Azam, "Microstrip patch antenna with defected ground structure for biomedical application," vol. 8, pp. 586–595, 2019.

[47] K. V. Kishore, G. S. Rajesh, V. Kumar, and P. Srinivasulu, "Design of 0.71λ, spacing 8-element microstrip patch antenna linear array for 0.43ghz wind profiling radar," in *2014 2nd International Conference on Emerging Technology Trends in Electronics, Communication and Networking*, Dec 2014, pp. 1–6.

[48] K. Kibaroglu, M. Sayginer, and G. M. Rebeiz, "An ultra low-cost 32-element 28 ghz phased-array transceiver with 41 dbm eirp and 1.0–1.6

gbps 16-qam link at 300 meters," in *2017 IEEE Radio Frequency Integrated Circuits Symposium (RFIC)*, June 2017, pp. 73–76.

[49] J. Huang, "A ka-band circularly polarized high-gain microstrip array antenna," *IEEE Transactions on Antennas and Propagation*, vol. 43, no. 1, pp. 113–116, Jan 1995.

[50] C. Deng, B. Yektakhah, and K. Sarabandi, "Series-fed dual-polarized single-layer linear patch array with high polarization purity," *IEEE Antennas and Wireless Propagation Letters*, vol. 18, no. 9, pp. 1746–1750, Sep. 2019.

[51] N. Ojaroudiparchin, M. Shen, S. Zhang, and G. F. Pedersen, "A switchable 3-d-coverage-phased array antenna package for 5g mobile terminals," *IEEE Antennas and Wireless Propagation Letters*, vol. 15, pp. 1747–1750, 2016.

JONAS MENDOZA (S'17) received the B.S. degree in electrical engineering from the University of Carabobo, Valencia, Venezuela, in 2012. Prior to joining the University of South Florida, Tampa, FL, USA, in 2017, He worked as an Application engineer and process optimization engineer for five years at SEW Eurodrive, 3M, and Empresas polar. Jonas got his M.S. degree in electrical engineering from the University of South Florida, Tampa, FL, USA, in 2019, where he is currently pursuing the Ph.D. degree in electrical engineering. His current research interests include RF devices reconfiguration using microfluidic actuation techniques.

MURAT KARABACAK (GS'11) received his B.S. and M.Sc. degrees in Electrical and Electronics Engineering from Istanbul University, Istanbul, Turkey in 2008 and 2010, respectively. He is currently pursuing his Ph.D. degree in Electrical Engineering at the University of South Florida. In 2013, he was with the research group of NTT Docomo Inc., CA, USA, as an intern where he was involved in the research of mobility, load balancing, analog beamforming in small cells. His research interests are physical and medium access control layer algorithms on mobility management, initial access, and self-organization in cellular networks for optimization of efficient control in wireless networks.

HÜSEYIN ARSLAN (Fellow, IEEE) received the B.S. degree from Middle East Technical University, Ankara, Turkey, in 1992, and the M.S. and Ph.D. degrees from Southern Methodist University, Dallas, TX, USA, in 1994 and 1998, respectively. From 1998 to 2002, he was with the Research Group, Ericsson Inc., NC, USA, where he was involved with several projects related to 2G and 3G wireless communication systems. Since 2002, he has been with the Electrical Engineering Department, University of South Florida, Tampa, FL, USA. He has also been the Dean of the College of Engineering and Natural Sciences, Istanbul Medipol University, since 2014. He was a part-time Consultant for various companies and institutions, including Anritsu Company, Morgan Hill, CA, USA, and The Scientific and Technological Research Council of Turkey (TÜBİTAK). His research interests include physical layer security, mmWave communications, small cells, multicarrier wireless technologies, co-existence issues on heterogeneous networks, aeronautical (high-altitude platform) communications, and in vivo channel modeling.

GOKHAN MUMCU (S'03–M'09–SM'15) was born in Bursa, Turkey, in 1982. He received the B.S. degree in electrical engineering from Bilkent University, Ankara, Turkey, in 2003, and the M.S. and Ph.D. degrees in electrical and computer engineering from The Ohio State University, Columbus, OH, USA, in 2005 and 2008, respectively. From 2009 to 2015, he was an Assistant Professor with the Electrical Engineering Department, University of South Florida, Tampa, FL, USA, where he is currently an Associate Professor with that department. His current research interests include small antennas, engineered materials, terahertz technologies, and reconfigurable RF devices, antennas and arrays using microfluidic reconfiguration techniques. Dr. Mumcu was a recipient of the 2014 CAREER Award from the U.S. National Science Foundation, the 2014 Faculty Outstanding Research Award from the University of South Florida, the Best Paper Award of the 2008 URSI National Radio Science Meeting, and the 2008 Outstanding Dissertation Award of The Ohio State University, ElectroScience Laboratory. He was the recipient of the 1999 International Education Fellowship of the Turkish Ministry of Education. He ranked first on the national university entrance exam taken annually by over 1.5 million Turkish students in 1999. He served as the Technical Program Committee Chair of the 2013 IEEE International Symposium on Antennas and Propagation and USNC/URSI National Radio Science Meeting and 2016 International Workshop on Antenna Technology.